NUMERICAL INVESTIGATION OF TURBULENT KINETIC ENERGY AND HEAT TRANSFER PERFORMANCE OF HIGH-POWER-DENSITY PERMANENT MAGNET SYNCHRONOUS MOTOR

by

Jiacheng ZHANG[a*], Baojun GE[a], and Haixu ZHANG[b]

[a]National Engineering Research Center of Large Electric Machines and Heat Transfer Technology (School of Electrical and Electronic Engineering, Harbin University of Science and Technology), Harbin, China
[b]Technology and Innovation Research Center, HIT Robot Group Co., Ltd, Taizhou, China

Original scientific paper
https://doi.org/10.2298/TSCI230402149Z

In the field of permanent magnet synchronous motors (PMSM) cooling, turbulent kinetic energy (TKE), and turbulent dissipation are used for the first time to numerically evaluate the heat transfer performance of axial water jackets, in order to investigate the influence of the water jackets structural parameters on the water-cooled system of high-power-density PMSM (HPD-PMSM). In the present work, the temperature distribution and fluid-flow pattern of a 40 kW HPD-PMSM were calculated using the finite element method, and temperature testing of the HPD-PMSM at different speeds using a built test platform. In addition, the effects of the bend shape of cooling channels (BSCC) on the axial water jackets performance for heat transfer are examined, and a detailed analysis of the mechanism underlying the development and evolution of high vorticity vortex is provided. The findings demonstrate that the TKE is attenuated by the positive vortex development, which is harmful to the TKE normal function in axial water jackets heat transfer. Furthermore, the maximum stator winding temperature was reduced to 93.49 °C and the maximum flow velocity within the water jackets could be increased by 14.34% owing to the BSCC improvement.

Key words*: HPD-PMSM, thermal management, axial water jacket, TKE, heat transfer performance, turbulent dissipation*

Introduction

The PMSM are used widely today in electric vehicles, aerospace, and other industries. This development has led to higher expectations for PMSM performance indicators, such as power density and efficiency, and has prompted the development of PMSM in the direction of HPD and light weight [1-3]. However, the increased power density means that the losses converted into heat energy will be greatly increased, leading to problems such as a sharp increase in the heat generation of the motor and irreversible demagnetization of the permanent magnets [4, 5]. Even worse, the high internal temperatures of the motor might hasten the pace of

*Corresponding author, e-mail: qingjide@foxmail.com

insulation material deterioration, which reduces the motor's lifespan [6]. As a result, HPD-PMSM thermal management is essential for both motor performance and operating safety [7, 8]. The water jacket (WJ) is one of the most attractive water-cooled approaches in PMSM due to the huge heat transfer contact surface and excellent heat transfer efficiency [9]. In this approach, casing and cooling channels make up the WJ, and the fluid removes heat by circulating in the cooling channels. The heat transfer performance of the WJ is influenced by factors such as structural parameters, flow velocity of the cooling channel and the nature of the cooling fluid. In the past few years, extensive research has been carried out on the heat transfer properties of the WJ.

To enhance the efficiency of PMSM multi-physics field coupled model building, Acquaviva *et al*. [10] proposed a new model to describe the thermal behavior of the motor, deriving a relationship between cooling channel diameter and convective heat transfer coefficient (CHTC), and providing a reference case for the structural design of the WJ by comparing the direct oil cooling scheme of the winding with the spiral WJ cooling scheme [11, 12]. Authors in [13-15] developed a thermal model of the PMSM based on CFD techniques and proposed improvements to the design method and design process for the spiral WJ, the relationship between the thermal characteristics of the rotor and factors such as WJ thickness was determined while increasing the peak power of the motor. Sun *et al*. [16] introduced an enhanced thermal management strategy for PMSM by designing the WJ as an inner and outer layer, with the inner layer set in the gap near the end windings, which reduced the maximum temperature of the motor by 23.6% while satisfying the accuracy.

In addition to exploring the heat transfer performance of WJ, many studies have also investigated the composition and feasibility of hybrid cooling systems for PMSM, using the WJ as an indispensable part of the cooling system [17-19]. To meet the cooling requirements of switched reluctance motors (SRM), Yan *et al*. [20] proposed a hybrid cooling system that consisted of air-cooled and water-cooled, and highlighted the Reynolds number of the cooling fluid as a key parameter for evaluating the thermal behavior of SRM [21]. To investigate the correlation between cooling system performance and maximum output torque, Authors in [22-24] integrated indirect cooling technique with direct cooling technique, determined the match between multiple cooling mediums, which provided a wealth of data to support the design of hybrid cooling for PMSM.

On the one hand, air, water, and oil cooling are all components of hybrid cooling systems. In this circumstance, the complex design process and the expensive cost of use restrict the application and promotion of hybrid cooling systems, aggravating the instability of the cooling system, and even some hybrid cooling systems sacrifice part of electromagnetic performance in exchange for increased cooling capacity. On the other hand, although there has been extensive research on WJ, most of them has remained on spiral WJ that are simple in design and have just enough heat transfer to meet the requirements, ignoring axial WJ that have the highest heat transfer efficiency, and most of the research has been on CHTC, Reynolds, and Nusselt numbers of WJ, especially in the design of heat transfer in PMSM [25-28]. As critical parameters that can measure the mass and heat transfer efficiency of WJ, TKE, and turbulent dissipation (TD) can be used to capture the degree of pulsation, kinetic energy changes, and the evolution of vortexes in the fluid field during WJ heat transfer. Moreover, to the authors' knowledge, there are no relevant studies on TKE and TD in the field of cooling of PMSM. Based on these findings, a 40 kW axial water-cooled HPD-PMSM prototype was manufactured, the finite element method was used to calculate the motor temperature distribution and fluid-flow pattern, the TKE distribution of the cooling fluid was investigated, a water-cooled HPD-PMSM test platform was built and the numerical results were compared with the experimental

results, thus verifying the validity of the 3-D finite element model. On this basis, the influence of BSCC on the heat transfer performance, TKE distribution, and degree of pulsation of axial WJ was investigated. The results of the present work provide new ideas for improving the thermal management of HPD-PMSM and research data for TKE-related calculations of axial WJ.

Numerical methods

Physical model

In this work, the 40 kW axially water-cooled HPD-PMSM is used as the study object and the detailed parameters of the prototype motor are given in tab. 1.

Table 1. Detailed parameters of the prototype motor

Parameter	Value	Parameter	Value
Rated power [kW]	40	Number of stator slots	36
Peak power [kW]	80	Number of poles	6
Rated rotational speed [rpm]	4000	Insulation class	H
Peak rotational speed [rpm]	9000	External diameter of stator[mm]	260
Rated torque [Nm]	120	Peak torque [Nm]	280

To obtain the steady-state temperature distribution and fluid-flow pattern of the motor, the 3-D finite element model shown in fig. 1(a) was created and solved in this work, fig. 1(b) illustrates the axial WJ calculation domain.

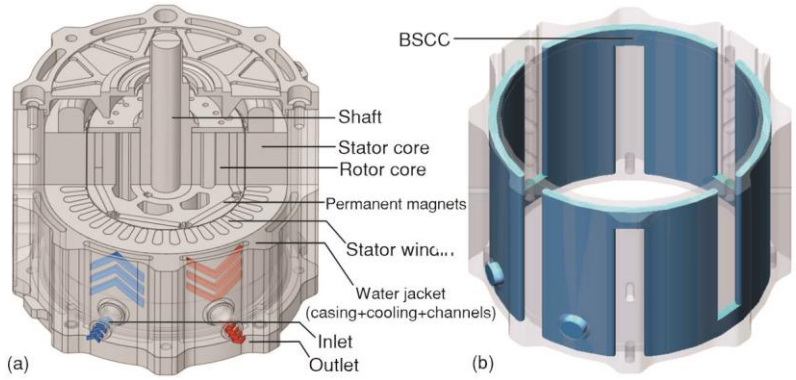

Figure 1. (a) 3-D finite element model and (b) axial WJ calculation domain

The thermal properties of the materials used in the HPD-PMSM are determined by the properties of the materials themselves, as shown in tab. 2.

Mesh generation

Figure 2 shows the HPD-PMSM co-nodal grids generated based on the poly-hexcore method, with details of the grid discretization as shown in the enlarged figure. Compared to tetrahedral grids generated using other methods, the hexahedral co-nodal grids generated based on the poly-hexcore method provide a low distortion, high quality mesh discretization scheme, thus ensuring accuracy in the calculation of the thermal behavior of the HPD-PMSM. The 3-D finite element model has a mesh count of 15.36 million, with 1.43 million in the WJ calculation area.

Table 2. Thermal properties of the materials of the HPD-PMSM

Parts of the motor	Materials	Thermal conductivity [W°C^{-1}]	Specific heat capacity [Jkg^{-1}°C^{-1}]	Density [kgm^{-3}]
Permanent magnets	N38UH	8	504	8400
Rotor core	SMC	21	450	7500
Stator core	Silicon lamination	4.5, 42.5	502	7650
Stator windings	Copper	387.6	381	8979
Cooling fluids	Water	0.6	4182	998

Thermal analysis

In this work, the temperature distribution and the flow pattern in the prototype motor are numerically calculated using the finite element method, with water being used as the cooling fluid within the WJ. In addition, the influence of different BSCC on the heat transfer performance of the WJ was investigated by improving the BSCC. In the analysis, the 3-D finite element model has the same dimensions as the prototype motor. To make the basic assumptions more realistic, it is assumed that the motor is well insulated. Other assumptions are:

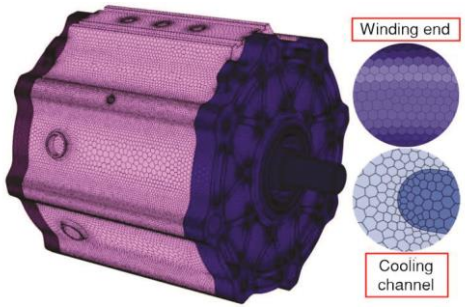

Figure 2. The HPD-PMSM hexahedral co-node mesh

– The air inside the motor and the cooling water inside the WJ, they flow at much less than the speed of sound and therefore the fluid is considered incompressible.
– The turbulence model is used to solve the flow field due to the high Reynolds number of the fluid in the motor.
– Cooling water enters the inlet of the axial WJ at a vertical angle.

To control fluid-flow in the fluid-solid coupled heat transfer model, the mass conservation is given as:

$$\frac{\partial \rho}{\partial t}+\frac{\partial(\rho \boldsymbol{u})}{\partial x}+\frac{\partial(\rho \boldsymbol{v})}{\partial y}+\frac{\partial(\rho \boldsymbol{w})}{\partial z}=0 \tag{1}$$

where ρ is the fluid density, t – the time, $\boldsymbol{u}$, $\boldsymbol{v}$, and $\boldsymbol{w}$ are the fluid velocity.

The flow of cooling fluid in the WJ and cooling pipes shall also conform to the law of conservation of momentum, which is given by:

$$\begin{aligned}
\frac{\partial(\rho \boldsymbol{u})}{\partial t}+\operatorname{div}(\rho u u) &= -\frac{\partial p}{\partial x}+\frac{\partial \tau_{xx}}{\partial x}+\frac{\partial \tau_{yx}}{\partial y}+\frac{\partial \tau_{zx}}{\partial z}+F_x \\
\frac{\partial(\rho \boldsymbol{v})}{\partial t}+\operatorname{div}(\rho v u) &= -\frac{\partial p}{\partial y}+\frac{\partial \tau_{xy}}{\partial x}+\frac{\partial \tau_{yy}}{\partial y}+\frac{\partial \tau_{zy}}{\partial z}+F_y \\
\frac{\partial(\rho \boldsymbol{w})}{\partial t}+\operatorname{div}(\rho w u) &= -\frac{\partial p}{\partial z}+\frac{\partial \tau_{xz}}{\partial x}+\frac{\partial \tau_{yz}}{\partial y}+\frac{\partial \tau_{zz}}{\partial z}+F_z
\end{aligned} \tag{2}$$

where i is the co-ordinate direction, F_i – the volume force on the microelement, p – the static pressure on the fluid microelement, τ_{xx}, τ_{xy}, and τ_{xz} are the viscous stress components on the surface of the microelement.

The heat transfer process during motor operation shall comply with the law of conservation of energy, which is described as:

$$\frac{\partial(\rho T)}{\partial t} + \mathrm{div}(\rho \boldsymbol{u} T) = \mathrm{div}\left(\frac{k}{c_P}\mathrm{grad}T\right) + S_T \tag{3}$$

where c_p is the specific heat capacity, T – the temperature of the fluid, k – the heat transfer coefficient of the fluid, and S_T – the fluid heat source.

The heat generated by the electromagnetic loss is mainly transferred to the outside of the motor via the axial WJ, where the heat sources come from the stator iron loss, winding copper loss, rotor iron loss and permanent magnet eddy current loss of the HPD-PMSM. The distribution of heat source densities at rated operation of the prototype motor is shown in tab. 3.

Table 3. Heat source densities of the prototype motor at rated operation

Parts of the motor	Rated loss [W]	Heat source density [Wm^{-3}]
Stator core	724	787569.4
Stator windings	916	948614.2
Permanent magnets	12.8	23743.6
Rotor core	203	127485.9

Turbulent kinetic energy analysis

The TKE is a parameter that describes the intensity of turbulence, and as a key parameter to measure the efficiency of mass and heat transfer in the WJ, it is directly related to the fluid momentum, heat transport within the WJ. These physical processes determine the ability of a fluid's flow state to develop into turbulent flow.

The TKE is defined by the following equation:

$$K = \frac{\int_{v_i}^{+\alpha} \rho k \mathrm{d}v}{m_i} \tag{4}$$

where $m_i = \rho V_i$ and K are the average TKE under mass weights, m_i – the mass of fluid and V_i – the volume of fluid in the calculation area.

The TD is the rate of conversion from TKE to kinetic energy of molecular thermal motion under molecular viscosity, measured by the TKE lost per unit mass of fluid per unit time.

The TD is defined by:

$$\varepsilon = \frac{\int_{v_i} \rho \dot{\varepsilon} \mathrm{d}v}{m_i} \tag{5}$$

where ε is the average TD under mass weights, $\dot{\varepsilon}$ – the TD.

Considering the working conditions for the rated operation of the HPD-PMSM and taking into account the characteristics of the axial WJ cooling structure, the outer wall surface of the casing is considered as the boundary condition for natural convection. The other necessary boundary conditions are as:

– The inlet of the axial WJ is defined as the velocity inlet and the outlet as the pressure outlet.
– The cooling water temperature and flow velocity at the inlet of the axial WJ were maintained at 45 °C and 1.3 m/s, respectively, and subsequently changed as the numerical simulation progressed.

– Based on the actual operating conditions of the HPD-PMSM, the rotor outer wall surface is defined as a rotating wall surface with an initial speed of 4000 rpm, which subsequently changes as the numerical simulation proceeds.

Experimental verification

To verify the accuracy of the theoretical analysis and numerical simulations, a 40 kW rated HPD-PMSM with axial WJ circulating water-cooled was manufactured, and the tested HPD-PMSM and test platform are shown in fig. 3. A comparison of the HPD-PMSM test results with the simulation results is shown in figs. 4(a) and 4(b).

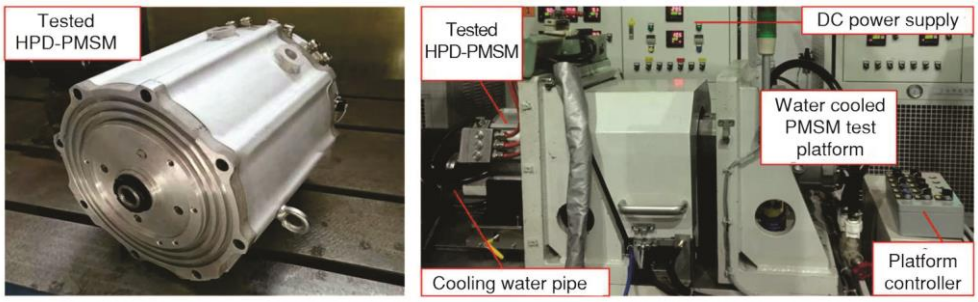

Figure 3. Tested HPD-PMSM and test platform

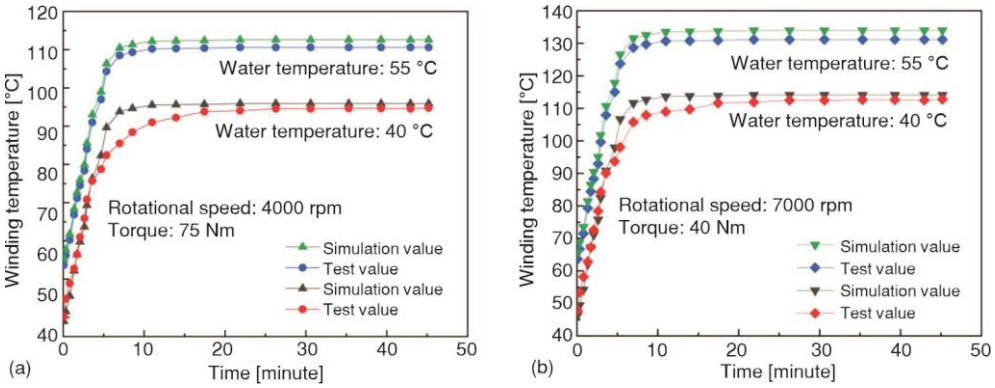

Figure 4. Comparison of test results with simulation results at; (a) 4000 rpm, 75Nm and (b) 7000 rpm, 40Nm

The tested HPD-PMSM is powered by the DC power supply cabinet and the motor output torque and speed are regulated by the platform controller. A thermostatic water tank, water pump and cooling water pipes make up the cooling supply system for the test motor. The temperature of the cooling water is controlled by the thermostatic water tank within a fluctuation range of 1.5 °C. The thermostatic water tank has thermometers placed at the inlet and outlet to measure the water temperature. To measure the winding temperature, a PT1000-2B platinum thermistor temperature sensor was placed on the inside of the winding end, the data collected was recorded by a computer and the ambient temperature was 29 °C during the test. In order to ensure experimental accuracy, different experimental conditions were set up for motor temperature testing, as shown in tab. 4.

In addition, from the fifth to the tenth minute of the test, there were significant differences between the test results and the simulated results, especially at 4000 rpm and 75 Nm. This

is due to the difference in boundary conditions resulting in numerical calculations with slower temperature growth rates. Fortunately, this error can be eliminated by more realistic boundary conditions, so the data fit of the test results to the simulation results gradually improves. After the maximum temperature of the winding has reached steady state, the maximum error between the test results and the simulation results is within 3%, all within reasonable limits, proving the effectiveness of the 3-D finite element model and the accuracy of the numerical calculations.

Table 4. Specific experimental conditions

Motor speed [rpm]	Output torque [Nm]	Water temperature at the WJ inlet [°C]	Flow velocity at the WJ inlet [ms^{-1}]
4000	75	40	1.3
4000	75	55	1.3
7000	40	40	1.3
7000	40	55	1.3

Results and discussion

Flow and heat transfer characteristics

Figures 5(a)-5(c) show the velocity vector distribution, the TKE distribution and the TD distribution of the cooling fluid in the axial WJ, respectively. The velocity distribution in

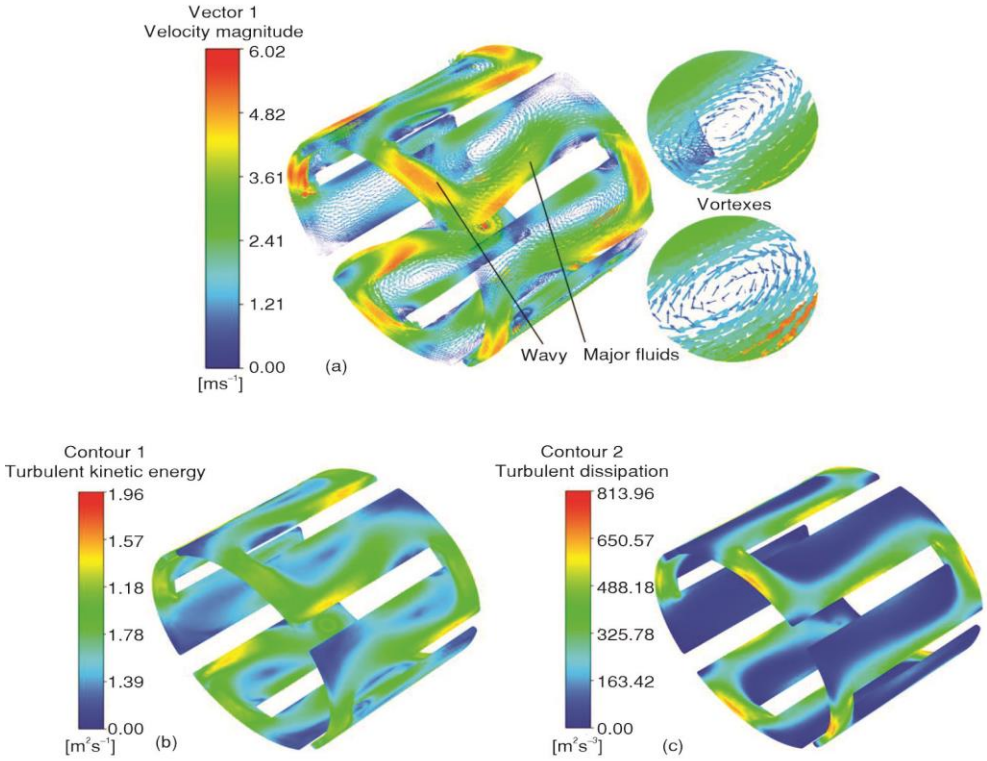

Figure 5. (a) Velocity vector distribution, (b) TKE distribution, and (c) TD distribution of fluids within the axial WJ

each cooling channel is very similar to the TKE distribution. The TKE showed a clear energy step near the bend in each cooling channel, while the maximum flow velocity and maximum TKE were also found near the bend. This is due to the fact that the viscous shear of the wall in the straight area of each cooling channel reduces the root mean square (RMS) amplitude of flow velocity, while the major fluids velocity near the bend increases the RMS amplitude of flow velocity, resulting in a large difference in the RMS amplitude.

Furthermore, it can be inferred from the distribution of the velocity vectors that, since the maximum flow velocity is located near the bend of the cooling channels, it means that wavy major fluids with high vorticity are distributed here. At the same time, vortexes with different vorticity are distributed at the front and back ends of the wavy major fluid, *i.e.* in the straight area of each cooling channel. With the interaction of vortexes of different vorticity and wavy major fluids, the degree of pulsation in the fluid field gradually increases, especially at the bends of each cooling channel where the pulsation peaks.

Additionally, the TD distribution is generally consistent with that of the TKE, with the TD peaks occurring at the bend of each cooling channel. In addition, as the cooling fluid-flows out from the bend in the cooling channels, the vorticity of the wavy major fluid tends to decrease, further indicating that small-scale vortexes will develop and evolve into large-scale vortexes, which in turn will cause the TKE to decay and ultimately change the TD distribution of the fluid field. It is worth noting that vortexes with high vorticity can disrupt the flow pattern of the fluid, which results in an attenuation of the TKE, detrimental to the proper heat transfer of the WJ.

By calculating the temperature field of the HPD-PMSM under rated operating conditions, the maximum temperature distribution of each part of the prototype motor was obtained as shown in fig. 6. The highest and secondary high temperature is located in the stator windings and permanent magnets respectively, with a maximum temperature of 95.89 °C and secondary high temperature of 92.13 °C.

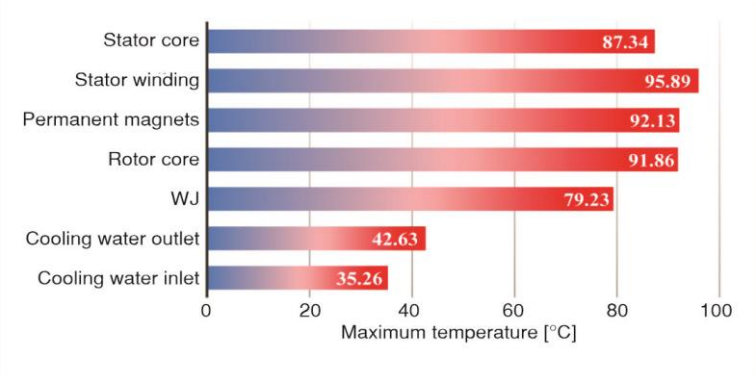

Figure 6. Maximum temperature for each part of the prototype motor

Influence of BSCC on heat transfer

To further investigate the influence of the axial WJ structural parameters on the heat transfer of the HPD-PMSM, the calculation process is shown in fig. 7.

In order to improve the flow pattern of the cooling fluid and to suppress the positive development of the vortexes in the cooling channels, this work is based on the original BSCC

(Scheme 1), and two other BSCC, Scheme 2, and Scheme 3, have been designed. Additionally, Considering the distance between the bend and the inlet and outlet of the axial WJ, the fourth bend was taken as the object of study. The specific locations of Line 1-Line 3 and Point 1-Point 29 in Scheme 1, Scheme 2, and Scheme 3 are given in figs. 8(a)-8(c), respectively. The TKE variations of Point 1-Point 29 under each scheme are shown in figs. 9(a)-9(c), respectively.

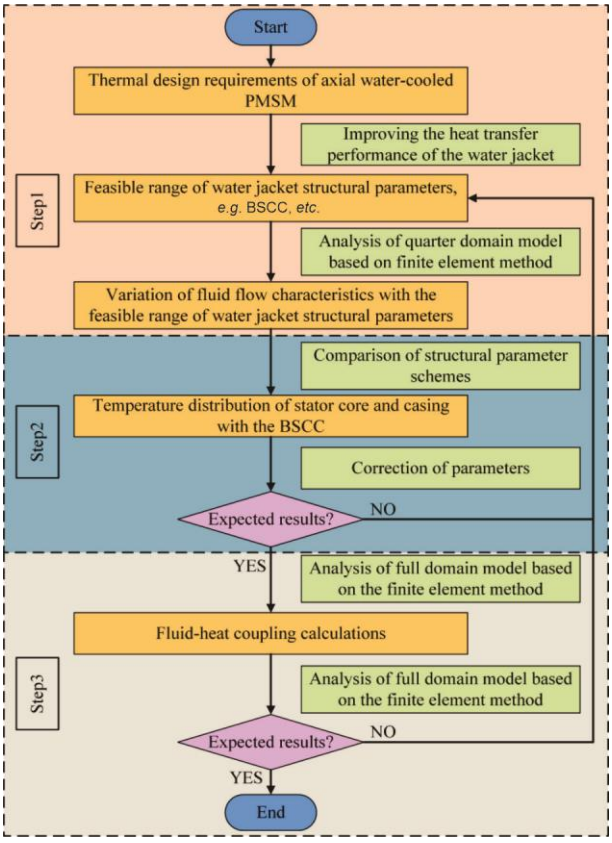

Figure 7. Calculation process

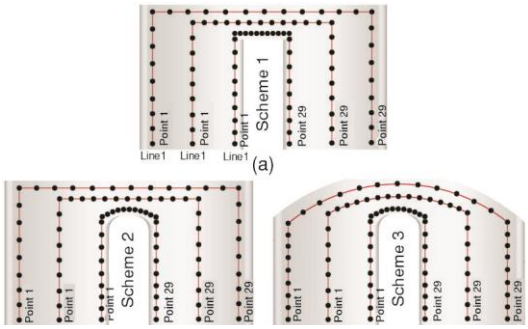

Figure 8. The specific location of Line 1-Line 3 and Point 1-Point 29 in; (a) Scheme 1, (b) Scheme 2, and (c) Scheme 3

With the improvement of BSCC, the peak TKE on Line 1 showed an increasing trend, the peak TKE on Line 2 and Line 3 showed a decreasing trend, and the peak TKE all appeared in the region around Point 20. Compared to Scheme 1, the TKE peaks on Line 1 for Scheme 2 and Scheme 3 increased by 5.82% and 60.85%, respectively, and the range of decrease in TKE peaks on Line 2 and Line 3 was 45.63-49.69%.

A comparison of the data clearly reveals that the improvement in BSCC has a greater influence on the TKE around Line 1,

with a gradual decrease in the number of energy steps occurring in the TKE near Line 2 and Line 3. The amplitude of the TKE at the bend is greater, which also means that the TD changes more dramatically at this location. It can be deduced that with the reduction of the right-angle structure at the bend, the vorticity of the wavy major fluid will further increase, the flow pattern of the fluid after the exit from the bend will improve and will eventually suppress the formation of high vorticity vortex.

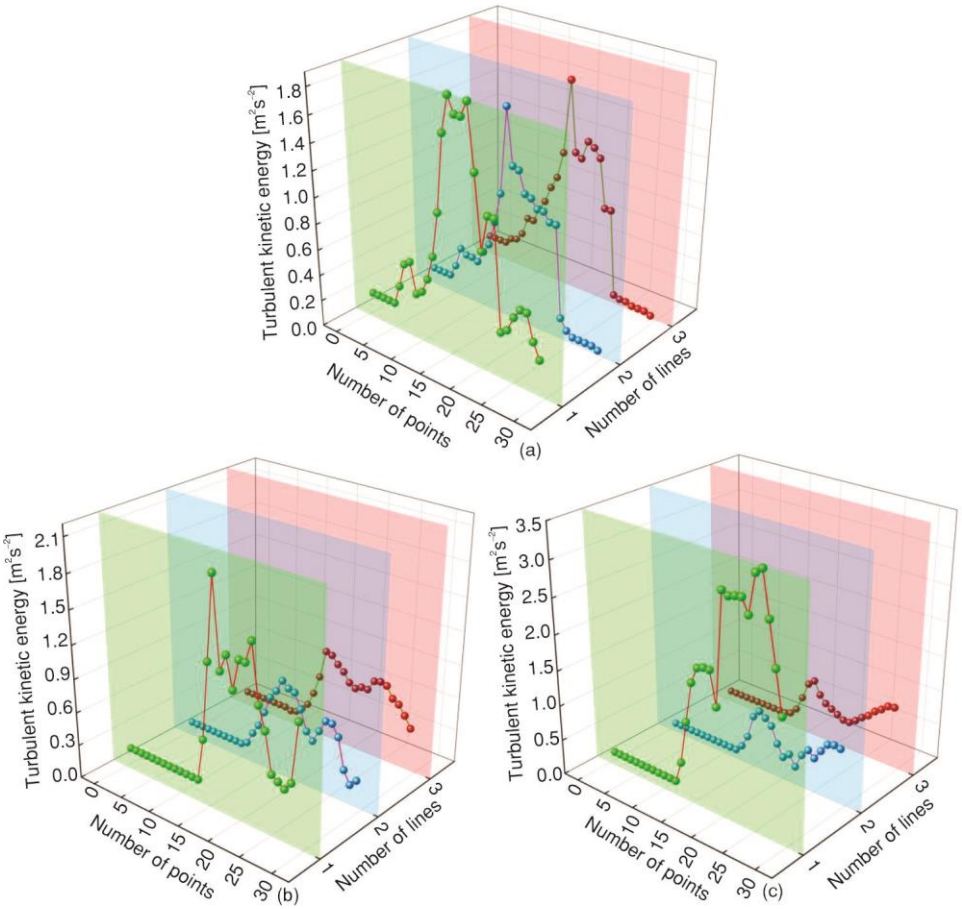

Figure 9. The Point1-Point29 TKE variations in;
(a) Scheme 1, (b) Scheme 2, and (c) Scheme 3

Figures 10(a)-10(c) show the distribution of fluid velocity vectors for Scheme 1, Scheme 2, and Scheme 3. With the improved BSCC, the peak flow velocity is still located at the bend, but compared to Scheme 1, the maximum flow velocity for Scheme 2 and Scheme 3 have increased by 0.93% and 14.34%, respectively. As the fluid-flows out of the bend, the positive development of the vortex with high vorticity is broken as the flow distance increases, and the integrity of the vortex is disintegrated. This also verifies the aforementioned deduction that the vorticity of the wavy major fluid increases further, the formation of high vorticity vortex is suppressed and the heat transfer performance of the axial WJ is further enhanced.

Figure 11 shows the stator temperature distribution for the prototype motor (BSCC = Scheme 1) and fig. 12 demonstrates the distribution of the maximum radial temperature for the

prototype motor in each scheme. In each scheme, the temperature distribution of the stator core shows a radially decreasing trend, the sequence of radial heat transfer is as follows: stator winding, stator core, axial WJ. With scheme1, the maximum stator winding temperature is 95.89 °C. Compared to Scheme 1, the maximum stator winding temperature is reduced by 0.9 °C and 2.4 °C for Scheme 2 and Scheme 3, respectively.

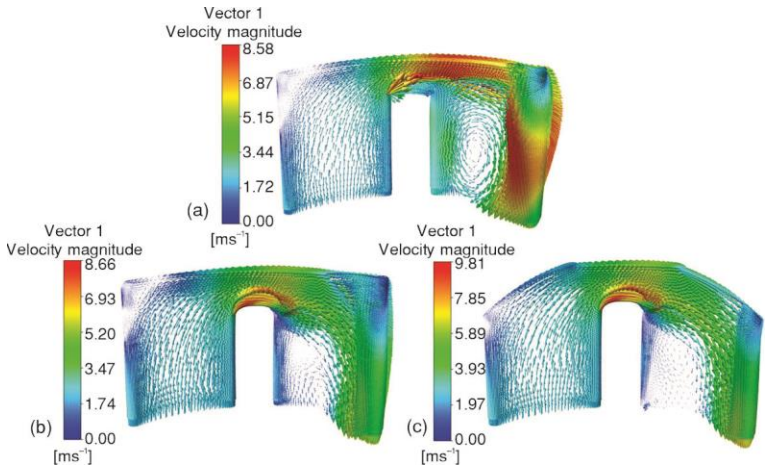

Figure 10. Velocity vector distribution of the fluid in; (a) scheme1, (b) scheme2 and (c) scheme3

Figure 11. Temperature distribution of the stator of the prototype motor

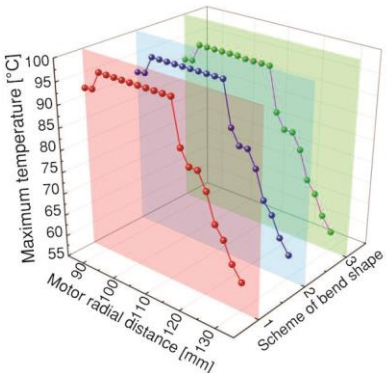

Figure 12. Maximum radial temperatures distribution of in each scheme

Conclusions

In the present work, the heat transfer characteristics of the axial WJ of the prototype were experimentally investigated, and the influence of the BSCC on the performance of the HPD-PMSM water-cooled system was investigated in detail. The following key findings are summarized from the present work:

- The flow velocity distribution in each cooling channel is very similar to the TKE distribution, with a clear energy step in the TKE near each bend, and the peak of both the flow velocity and TKE distributed around the bend. With the interaction of vortexes of different vorticity and wavy major fluids, the TD in the fluid field gradually increases, especially at the bends of each cooling channel where the TD peaks.

- As the cooling fluid-flows out of the bend in the cooling channels, the vorticity of the wavy major flow fluid to decrease. The small-scale vortexes evolve into large scale vorticity, which results in TKE decay and ultimately has a detrimental influence on the heat transfer performance of the axial WJ.
- The improvement of BSCC can increase the vorticity of the wavy major fluid further, the formation of high vorticity vortex is suppressed, the heat transfer performance of the axial WJ is further enhanced and fluid siltation has been significantly reduced. Compared to scheme1, the maximum flow velocity of scheme2 and scheme3 increase by 0.93% and 14.34% respectively, and the maximum stator winding temperatures decrease by 0.9°C and 2.4°C respectively.

References

[1] Giangrande, P., *et al*., Considerations on the Development of an Electric Drive for a Secondary Flight Control Electromechanical Actuator, *IEEE Trans. on Industrial Electronics, 55* (2019), 4, pp. 3544-3554
[2] Bramerdorfer, G., *et al*., Modern Electrical Machine Design Optimization: Techniques, Trends, and Best Practices, *IEEE Transactions on Industrial Electronics, 65* (2018), 10, pp. 7672-7684
[3] Wenming, T., *et al*., Loss and Thermal Analysis for High-Speed Amorphous Metal PMSMs Using 3-D Electromagnetic-thermal Bi-Directional Coupling. *IEEE Transactions on Energy Conversion, 36* (2021), 4, pp. 2839-2849
[4] Lu, Q., *et al*., Modeling and Investigation of Thermal Characteristics of a Water-Cooled Permanent-Magnet Linear Motor, *IEEE Transactions on Industry Applications, 51* (2018), 3, pp. 2086-2096
[5] Li., B., *et al*., Cooling Structure Design for an Outer-Rotor Permanent Magnet Motor Based on Phase Change Material, *Thermal Science and Engineering Progress, 34* (2022), 101406
[6] He, H., *et al*., Efficiency Decrease Estimation of a Permanent Magnet Synchronous Machine with Demagnetization Faults, *Energy Procedia, 105* (2017), 5, pp. 2077-2087
[7] Sun, Y., *et al*., Experimental and Numerical Investigation on a Novel Heat Pipe Based Cooling Strategy for Permanent Magnet Synchronous Motors, *Applied Thermal Engineering, 170* (2020), 114970
[8] Tikadar, A., *et al*., Comparison of Electro-Thermal Performance of Advanced Cooling Techniques for Electric Vehicle Motors, *Applied Thermal Engineering, 183* (2021), 116182
[9] Zhao, J., *et al*., Design and Optimization of Water Cooling System for High Power Density Permanent Magnet Motor Based on Multi-Physics Field Simulation, *Proceedings,* 1st IEEE Student Conference on Electric Machines and Systems, IEEE SCEMS, Huzhou, China, 2018
[10] Acquaviva, A., *et al*., Computationally Efficient Modeling of Electrical Machines with Cooling Jacket, *IEEE Transactions on Transportation Electrification, 5* (2019), 3, pp. 618-629
[11] Wu, S., *et al*., Design and Optimization Analysis of Composite Water Cooling System Based on High Power Density Motor, *Proceedings,* 22nd Int. Con. on Electrical Machines and Systems, ICEMS, Harbin, China, 2019
[12] Petrov, I., *et al*., Investigation of a Direct Liquid Cooling System in a Permanent Magnet Synchronous Machine, *IEEE Transactions on Energy Conversion, 35* (2020), 2, pp. 808-817
[13] Han, J., *et al*., Influence of Electric Shield Materials on Temperature Distribution in the End Region of a Large Water-Hydrogen-Hydrogen-Cooled Turbogenerator, *IEEE Transactions on Industrial Electronics, 67* (2020), 5, pp. 3431-3441
[14] Du, G., *et al*., Power Loss and Thermal Analysis for High-Power High-Speed Permanent Magnet Machines. *IEEE Transactions on Industrial Electronics, 67* (2019), 4, pp. 2722-2733
[15] Chang, J., *et al*., A Yokeless and Segmented Armature Axial Flux Machine with Novel Cooling System for In-Wheel Traction Applications, *IEEE Trans. on Ind.l Ele., 68* (2021), 5, pp. 4131-4140
[16] Sun, Y., *et al*., Applicability Study of the Potting Material Based Thermal Management Strategy for Permanent Magnet Synchronous Motors, *Applied Thermal Engineering, 149* (2018), Feb., pp. 1370-1378
[17] Lundmark, S. T., *et al*., Coupled 3-D Thermal and Electromagnetic Modelling of a Liquid-cooled Transverse Flux Traction Motor, *Proceedings,* XIII Int. Con. on Electrical Machines (ICEM), Alexandroupoli, Greece, 2018
[18] Chen, X., *et al*., Thermal Modeling of Hollow Conductors for Direct Cooling of Electrical Machines, *IEEE Transactions on Industrial Electronics, 67* (2020), 2, pp. 895-905

[19] Gai, Y., *et al*., Numerical and Experimental Calculation of CHTC in an Oil-Based Shaft Cooling System for a High-Speed High-Power PMSM, *IEEE Trans. on Industrial Electronics, 67* (2020), 6, pp. 4371-4380
[20] Yan, W. M., *et al*., Electromagnetic Field Analysis and Cooling System Design for High Power Switched Reluctance Motor, *Int. J. of Numerical Methods for Heat & Fluid-flow, 29* (2019), 5, pp. 1756-1785
[21] Chiu, H. C., *et al*., Thermal Performance Analysis of a 30 kW Switched Reluctance Motor, *International Journal of Heat and Mass Transfer, 114* (2017), Nov., pp. 145-154
[22] Lindh, P., *et al*., Direct Liquid Cooling Method Verified with an Axial-Flux Permanent-Magnet Traction Machine Prototype, *IEEE Transactions on Industrial Electronics, 64* (2017), 8, pp. 6086-6095
[23] Acquaviva, A., *et al*., Design and Verification of In-Slot Oil-Cooled Tooth Coil Winding PM Machine for Traction Application, *IEEE Transactions on Industrial Electronics, 68* (2020), 5, pp. 3719-3727
[24] Vansompel, H., *et al*., Extended End-Winding Cooling Insert for High Power Density Electric Machines with Concentrated Windings, *IEEE Trans. on Energy Conversion, 35* (2020), 2, pp. 948-955
[25] Pei, B. B., *et al*., Flow and Heat Transfer of Supercritical CO_2 in the Honeycomb Ultra-Compact Plate Heat Exchanger, *The Journal of Supercritical Fluids, 148* (2019), June, pp. 1-8
[26] Zhang, X. T., *et al*., Study on Convection Heat Transfer of End-Winding for a 10 kW External Rotor PMSM With Open End Cap, *IEEE Transactions on Energy Conversion, 37* (2022), 3, pp. 1934-1945
[27] Chen, W., *et al*., Design and Optimization of Dual-Cycled Cooling Structure for Fully-Enclosed Permanent Magnet Motor, *Applied Thermal Engineering, 152* (2019), Apr., pp. 338-349
[28] Jang, J. H., *et al*., Numerical Study on Electromagnetic and Thermal Cooling of a Switched Reluctance Motor, *Case Studies in Thermal Engineering, 6* (2015), Sept., pp. 16-27

Paper submitted: April 2, 2023
Paper revised: May 16, 2023
Paper accepted: May 18, 2023